# RSC Advances

ROYAL SOCIETY OF CHEMISTRY

www.rsc.org/advances

# Solution-processed high-efficiency p-NiO/n-ZnO heterojunction photodetector

*Ratan Debnath, [†],[*] Ting Xie, [†],[§] Baomei Wen, [†],[Δ] Wei Li, [∈],[£] Jong Y. Ha, [†],[¥] Nichole F. Sullivan,[Δ] Nhan V. Nguyen[∈] and Abhishek Motayed[†],[¥]*

[†]Materials Science and Engineering Division, Material Measurement Laboratory, National Institute of Standards and Technology, Gaithersburg, MD 20899 USA

[Δ]N5 Sensors Inc., Rockville, MD 20852 USA

[§]Department of Electrical and Computer Engineering, University of Maryland, College Park, MD 20742, USA

[¥]Institute for Research in Electronics and Applied Physics, University of Maryland, College Park, MD 20742 USA

[∈]Semiconductor and Dimensional Metrology Division, Physical Measurement Laboratory, National Institute of Standards and Technology, Gaithersburg, MD 20899 USA

[£]Key Laboratory for the Physics and Chemistry of Nano Devices, Peking University, Beijing, China

**Abstract**

This paper presents a high efficiency heterojunction p-NiO/n-ZnO thin film ultraviolet (UV) photodetector (PD) fabricated on conductive glass substrates. The devices are fabricated by using

a simple spin-coating layer-by-layer method from precursor solutions. Photodiodes show good photoresponse and quantum efficiency under UV illumination. With an applied reverse bias of 1 V, the devices show maximum responsivity and detectivity of 0.28 A/W and 6.3 x $10^{11}$ Jones, respectively, as well as high gain with external quantum efficiency (EQE) of over 90%. By employing ultrathin Ti/Au as top UV transparent metal contacts, this architecture allows the PDs to be illuminated either through glass or metal side. Laser beam induced current is used to examine the local variation of EQE providing information on the photoresponse behavior within the device. Optical properties of NiO and ZnO deposits have also been explored.

**Keywords:** NiO, ZnO, photodetector, TMO

## 1. Introduction

Transition-metal oxides (TMOs) have attracted attention among the research community due to unique material properties.[1-5] They have also been utilized for various device applications[6-8] as alternatives to silicon and other wide-bandgap inorganic semiconductors such as SiC, GaN etc. that require expensive vacuum system for deposition. Among various TMOs, ZnO and NiO thin films are of particular interest. ZnO is widely studied for applications such as light emitting diodes (LEDs),[9] solar cells,[10] chemical sensors,[11] nanogenerator,[12] photodetectors,[13] thin-film transistor,[14] and memory devices.[15] NiO has been used in LEDs,[16] resistive memory switching,[17, 18] and photovoltaics.[19] NiO and ZnO are intrinsically p- and n-type semiconductors, respectively, and their band alignments make them promising candidates for heterojunction thin film devices for optoelectronic applications such as LEDs[20] and photodetectors (PDs).[21-25] In most cases, NiO and ZnO thin films have been deposited via pulsed laser deposition,[26, 27] sputtering[28, 29] or chemical vapor deposition,[30, 31] all expensive, energy intensive, high vacuum deposition process.

Non-vacuum processes such as solution-based material synthesis can be an alternative route for low-cost, large area, high throughput thin film deposition. Recently, there have been several reports of ultraviolet (UV) PDs utilizing these oxides from sol-gel processing[24, 25] in parallel with other wide bandgap materials.[32-34]

In this paper, we have fabricated UV PDs from transparent layers of NiO and ZnO spin-coated from a sol-gel solution. The devices are fabricated on low-cost fluorine-doped tin oxide (FTO) coated glass substrates rather than indium-doped tin oxide, which allows annealing at high temperature although they are processed at relatively low temperature. UV transparent top metal contacts are engineered allowing illumination of devices through both the glass/FTO and top metal contacts. Finally, the performance of the PDs are measured to demonstrate high external quantum efficiency (EQE) and responsivity.

## 2. Experimental Details

### 2.1 Precursor solution

For NiO, nickel acetate tetrahydrate was dissolved in 2-methoxyethanol and monoethanolamine (MEA) in a glass vial. Similarly, ZnO precursor solution was prepared separately using zinc acetate tetrahydrate in the same solvents. The molar ratio of $Ni^{2+}/Zn^{2+}$:MEA was maintained at 1:1 in the solution. The dissolved precursors were magnetically stirred at 50 °C for 2 hours in a water bath and then filtered with a 0.45 μm filter.

### 2.2 Device Fabrication

The FTO/glass substrates were first cleaned with acetone and isopropanol in an ultrasonic bath and subsequently rinsed with deionized water, and finally dried with $N_2$ gas. For thin film

fabrication, NiO precursor was spin-coated on the FTO/glass substrates and the typical film thickness varied between 50 to 60 nm. The film was immediately dried at 150 °C for several minutes on a preheated hot plate in a fumehood. The procedure was repeated five times in order to achieve film thickness of 250 nm to 300 nm. The process was repeated for ZnO to obtain $\approx$ 70 nm to 80 nm thick film. Finally, the films were annealed at 300 °C for 30 min in air. Ti (5nm)/Au (5nm) top contacts were deposited by electron-beam evaporation at a rate of $\approx$ (0.5 - 1) Å/s through a metal mask having an array of circular openings of 4 mm and the finished devices were then finally annealed at 300 °C for 1 min in a $N_2$ environment using rapid thermal annealing. No process optimization is performed.

## 2.3 Characterization Methods

Surface morphology and cross-sectional structure of the PDs were examined using atomic force microcopy (AFM) and scanning electron microscopy (SEM). Devices were characterized for current-voltage (I-V) and EQE measurements using a spectrally filtered light source and the system was calibrated using a NIST-calibrated silicon photodiode. A total uncertainty of $\pm$ 5 % (fractional) is associated with measured EQE under AM1.5 illumination.

An integrated HORIBA Jobin Yvon's LabRAM 800HR bench-top system[*] was used for Raman spectroscopy (Laser Quantum DPSS, 532 nm) measurements with laser spot sizes of $\approx$ 1 µm. The local EQE measurements were collected using the same Raman microscope system equipped with a laser (Kimmon He-Cd, 325 nm). The beam was turned on a minimum of 20 min prior to use in order to ensure power stability during measurements. Vacuum ultraviolet variable

---

[*]Certain commercial equipment, instruments, or materials are identified in this paper in order to specify the experimental procedure adequately. Such identification is not intended to imply recommendation or endorsement by the National Institute of Standards and Technology, nor is it intended to imply that the materials or equipment identified are necessarily the best available for the purpose.

angle ellipsometry (VUV-VASE) measurements were performed to determine the dielectric functions of the films from which optical band gaps were extracted by employing Tauc plots.[35] Currents were monitored chronopotentiometrically with a CH Instruments potentiostat connected to the device by micromanipulator probes. The laser beam passed through a neutral density filter and 15× UV objective for focusing, and the light intensity at the device was measured with a Thor Laboratories PM100D laser power meter immediately after device measurements. Measured laser output power at the sample for these conditions was on the order of 6.5 μW. Total uncertainties on stated power are ± 3 % based on the measured change of beam intensity over the duration of the mapping experiments.

For mapping, the sample was scanned using a step size of 20 μm resolution to cover a 400 μm x 400 μm area. On the basis of an approximate beam diameter of 20 μm obtained from visual examination, local EQE in the device was estimated and thus the absolute values in the EQE maps reported here should not be considered directly comparable to standard EQE measurements.

## 3. Results and Discussion

Fig. 1 shows the cross-sectional SEM and top-view AFM images of annealed NiO and ZnO thin films. Both films have smooth surfaces and polycrystalline nanoscale grains. The AFM images manifest the relative surface smoothness of NiO and ZnO thin films and the measured mean square root roughness are estimated to be ≈ 0.5 nm and ≈ 2.3 nm, respectively. Such nanoscale surface roughness makes it suitable to fabricate abrupt heterojunctions in device applications.

Fig. 2a shows the Tauc plot of the thin films which is a linear relationship of $(\alpha h\upsilon)^2$ vs. photon energy where $\alpha$ is the absorption coefficient and $h\upsilon$ is the photon energy. The optical band gaps

are deduced from a linear fit to the near band gap spectral region and found to be $\approx$ 3.68 eV and $\approx$ 3.24 eV for NiO and ZnO, respectively. Thus, both films are highly transparent in the visible range making them suitable for UV PDs. The micro-Raman spectra in Fig. 2b was recorded using 532 nm excitation wavelength at room temperature. The bands observed at $\approx$ (460.3 $\pm$ 0.7) cm$^{-1}$ and $\approx$ (562.3 $\pm$ 0.5) cm$^{-1}$ can be ascribed to the transverse optical (TO) and longitudinal optical (LO) phonon modes of NiO, respectively. The peaks at $\approx$ (784.6 $\pm$ 0.5) cm$^{-1}$ and $\approx$ (1094.4 $\pm$ 0.3) cm$^{-1}$ correspond to 2TO and 2LO combination phonon modes. All these are in good agreement with the reported values of NiO.[36, 37] Similarly, the peaks at $\approx$ (431.1 $\pm$ 0.1) cm$^{-1}$ and $\approx$ (375.5 $\pm$ 0.1) cm$^{-1}$ are close to $E_2^{high}$ and A$_1$(TO) of ZnO.[38] XRD patterns of the films are shown in Fig. 2c. All diffraction peaks can be indexed to the cubic NiO (JCPDS-78-0643) or hexagonal ZnO structure (JCPDS 36-1451. The broad diffraction peaks are consistent with the small grain size and/or high defect density of material processed relatively at low temperature.

The band diagrams of the NiO/ZnO interface at steady state and under reverse bias are plotted in Fig. 3a using SCAPS-1D simulator.[39] At equilibrium, there is a space-charge region at the interfaces due to the diffusion of electrons and holes, and a built-in electrical field is created that assists in separation of electrons and holes. Under reverse bias, the depletion region of the junction increases and a very small net current flow across the device is expected. The I-V curve of the NiO/ZnO heterojunction diode reveals the anticipated rectifying behavior and exhibits a rectification ratio of $\approx$ 2200 at $\pm$ 1 V in the dark (Fig. 3b). Under UV illumination, current enhancement is observed under reverse bias. The increased currents result from the photogenerated carries within the junction. The photogenerated electrons are transported through the ZnO layer to the Ti/Au cathode and the holes are transported from the NiO to the FTO anode. The photoresponse factor (S) of the PD is defined as

$$S = \frac{I_{UV} - I_{dark}}{I_{dark}}$$

where $I_{UV}$ is the current under UV illumination and $I_{dark}$ is the dark current. The S for the

NiO/ZnO PDs is $\approx 2$ at a reverse bias of 1 V, similar to that of PDs based on oxides.[40-42]

Fig. 4a shows the EQE of a NiO/ZnO device under applied reverse bias. The illumination is through the FTO/glass side and the spectral response is measured by scaling the measured photocurrent with that of a Si photodetector, given nominally identical illumination. At a reverse bias of 1 V, the maximum EQE at 365 nm reaches to $\approx 93\%$ (Fig. 4a). The EQE of the detector is limited by the UV cut-off wavelength of the FTO anode and thus it gradually decreases to $\approx$ 0.3% at 320 nm. The responsivity ($R_\lambda$) which is the ratio of photocurrent and light intensity is approximately $\approx 0.28$ A/W at 365 nm (Fig. 4b). The heterojunction device exhibits excellent UV-selective sensitivity with a UV-to-visible rejection ratio ($R_{\lambda=365nm}/R_{\lambda=550nm}$) approaching $\approx 1500$. The specific detectivity ($D^*$), which is another figure of merit can be calculated assuming the dark current to be the major source of shot noise using the expression:

$$D^* = \frac{R_\lambda}{\sqrt{2qJ_{dark}}}$$

where $q$ is the electron charge, and $J_{dark}$ is the dark current at the same value of reverse bias used for $R_\lambda$.[24] The calculated detectivity at 365 nm reaches to a maximum of $6.3 \times 10^{11}$ Jones.

The device architecture also allows illumination through the Ti/Au ultrathin metal contacts permitting UV transmission as reported for other metal.[43] A PD response from this configuration is shown in Fig. 5a. The EQE reaches $\approx 57\%$ at 355 nm and the corresponding $R_\lambda$ and D* estimated to be 0.18 A/W and $4.1 \times 10^{11}$ Jones at 0.8 V, respectively. Although ultrathin Ti/Au

7

contacts likely absorb some UV light, but they are still more transparent as compared to FTO electrode in the UV regime (below 330 nm) and hence, the response of the PD is extended up to 300 nm. Overall, the figures of merit are quite reasonable as compared to those for bottom illumination.

In order to assess the spatial variation of device performance under UV illumination, we have mapped the photoresponse with a piezoelectric stage and a focused He-Cd 325 nm, 6.5 µW laser beam. The EQE estimated from the current under short circuit conditions (i.e., under zero bias) indicates $\approx$ 30% relative variation across the surface of this heterojunction device suggesting spatial variation of recombination (Fig. 5b). When the device is operated under reverse bias, there is significant increase of EQE as seen in Fig. 4a and Fig. 5a. It has been reported that NiO films fabricated this way contain $Ni_2O_3$ or $Ni(OH)_2$ as well as NiO when annealed at lower temperature.[25] That can act as trap sites in the NiO film. The gain in this photodiode has been correlated with the interfacial trap-controlled charge injection suggesting the annealing temperature plays a crucial role controlling defects and deviation from stoichiometry.

Fig. 5c shows the transient response of the fabricated photodetectors during 325 nm laser excitation switching. The photocurrent increases rapidly upon exposure to UV radiation and stays essentially constant during the UV exposure. The current responds far more slowly to the pre-exposure value after illumination is turned off. The rise time ($t_r$) for the photocurrent to reach 90% of its maximum value, is approximately 0.28 s. The decay time ($t_d$) for the photocurrent to decrease to 10% of the initial value, is 5.4 s. The values of $t_r$ and $t_d$ are as good or better than, other reported oxide based PDs.[40] The slow UV response and recovery can be attributed to the oxygen adsorption and desorption process.[13, 44, 45] In the dark, oxygen molecules adsorb on the ZnO surface, capturing free electrons from the n-ZnO [$O_2(g)+e^- \rightarrow O_2^-(ad)$]. As a

consequence, a low-conductivity depletion layer is created near the surface. When the device is illuminated by UV light having photon energies exceeding the band gap of the semiconductor, electron-hole pairs are generated. These photo-generated holes migrate to the surface and either discharge the adsorbed oxygen ions through surface electron-hole recombination to produce photo-desorbed oxygen gas $[O_2^- \text{ (ad)} + h^+ \rightarrow O_2 \text{ (g)}]$ or get trapped on the surface resulting in increased free carrier concentration and reduced depletion width. The unpaired electrons accumulate until adsorption and desorption of $O_2$ reaches in a steady state. Thus the current will keep on rising until it is saturated by the UV illumination. This hole-trapping mechanism can augment the traps residing in the semiconductor and enhance the photoresponse. When the UV illumination is turned off, holes recombine with the unpaired electrons, while oxygen gradually reabsorbs in the surface resulting in a slow current decay. The performance of PDs in this work and some previously reported data are summarized in Table 1 for comparison.

Other opportunities to explore these ideal TMO systems exist including investigation of materials properties and device performance under various environments. This may include UV ozone treatment on those oxide films, including its effect on oxygen vacancies as well as the change in metal-oxide work function as reported in the past.[46] This might assist the metal-semiconductor junction to extract the electron-holes to their respective contacts. Such treatment might also allow lowering the processing temperatures, similar to those for polymer solar cells,[46] congenial to fabrications of PDs on flexible substrates. Due to the ease of cost-effective solution-processing, one might also tune the bandgap by mixing with other appropriate oxides enabling devices with photodetection capability over a larger UV range.

**CONCLUSIONS**

In summary, we have demonstrated simple, cost-effective solution-processed UV photodetectors that can be conveniently fabricated on FTO/glass substrates by spin-coating using wide-band gap TMOs, viz. NiO and ZnO. The architecture allows illumination either through the top or bottom contact without significantly loss of device performance. The heterojunction diode exhibits very low dark current under reverse bias with an excellent on/off ratio suggesting low free carrier density. The PDs are manifested an impressive performance with maximum EQE of 93% as well as superior responsivity and detectivity in the UV regime. Photocurrent mapping using a monochromatic light source under zero bias depicts modest variation of the photoresponse across the device. The characteristic rise and fall times of the photocurrent are 0.28 s and about 5.4 s respectively, acceptable for applications not requiring high speeds. Considering the advantages of solution-processable fabrication, the devices have potential for use in large-area UV PD applications.

**Corresponding Author**

*E-mail: ratan.debnath@nist.gov

**Notes**

The authors declare no competing financial interest.

## References

1. A. Ohtomo and H. Y. Hwang, *Nature*, 2004, **427**, 423-426.
2. H. Y. Hwang, Y. Iwasa, M. Kawasaki, B. Keimer, N. Nagaosa and Y. Tokura, *Nat Mater*, 2012, **11**, 103-113.
3. M. Mostovoy, *Nat Mater*, 2008, **7**, 269-270.
4. D. Xiao, W. Zhu, Y. Ran, N. Nagaosa and S. Okamoto, *Nat Commun*, 2011, **2**, 596.
5. A. Tsukazaki, A. Ohtomo, T. Kita, Y. Ohno, H. Ohno and M. Kawasaki, *Science*, 2007, **315**, 1388-1391.
6. P. Poizot, S. Laruelle, S. Grugeon, L. Dupont and J. M. Tarascon, *Nature*, 2000, **407**, 496-499.
7. J. J. Yang, M. D. Pickett, X. Li, A. A. OhlbergDouglas, D. R. Stewart and R. S. Williams, *Nat Nano*, 2008, **3**, 429-433.
8. X. Lang, A. Hirata, T. Fujita and M. Chen, *Nat Nano*, 2011, **6**, 232-236.
9. A. Tsukazaki, A. Ohtomo, T. Onuma, M. Ohtani, T. Makino, M. Sumiya, K. Ohtani, S. F. Chichibu, S. Fuke, Y. Segawa, H. Ohno, H. Koinuma and M. Kawasaki, *Nat Mater*, 2005, **4**, 42-46.
10. M. Law, L. E. Greene, J. C. Johnson, R. Saykally and P. Yang, *Nat Mater*, 2005, **4**, 455-459.
11. R. Ahmad, N. Tripathy, D.-U.-J. Jung and Y.-B. Hahn, *Chemical Communications*, 2014, **50**, 1890-1893.
12. S. Xu, Y. Qin, C. Xu, Y. Wei, R. Yang and Z. L. Wang, *Nat Nano*, 2010, **5**, 366-373.
13. Y. Jin, J. Wang, B. Sun, J. C. Blakesley and N. C. Greenham, *Nano Letters*, 2008, **8**, 1649-1653.
14. K. Nomura, H. Ohta, A. Takagi, T. Kamiya, M. Hirano and H. Hosono, *Nature*, 2004, **432**, 488-492.
15. N. Xu, L. Liu, X. Sun, X. Liu, D. Han, Y. Wang, R. Han, J. Kang and B. Yu, *Applied Physics Letters*, 2008, **92**, 232112
16. J. M. Caruge, J. E. Halpert, V. Wood, V. Bulovic and M. G. Bawendi, *Nat Photon*, 2008, **2**, 247-250.
17. R. Waser and M. Aono, *Nat Mater*, 2007, **6**, 833-840.
18. K. Oka, T. Yanagida, K. Nagashima, H. Tanaka and T. Kawai, *Journal of the American Chemical Society*, 2009, **131**, 3434-3435.
19. E. A. Gibson, A. L. Smeigh, L. Le Pleux, J. Fortage, G. Boschloo, E. Blart, Y. Pellegrin, F. Odobel, A. Hagfeldt and L. Hammarström, *Angewandte Chemie*, 2009, **121**, 4466-4469.
20. Y. Y. Xi, Y. F. Hsu, A. B. Djurišić, A. M. C. Ng, W. K. Chan, H. L. Tam and K. W. Cheah, *Applied Physics Letters*, 2008, **92**, 113505.
21. H. Ohta, M. Hirano, K. Nakahara, H. Maruta, T. Tanabe, M. Kamiya, T. Kamiya and H. Hosono, *Applied Physics Letters*, 2003, **83**, 1029-1031.
22. S.-Y. Tsai, M.-H. Hon and Y.-M. Lu, *Solid-State Electronics*, 2011, **63**, 37-41.
23. Y. Vygranenko, K. Wang and A. Nathan, *Applied Physics Letters*, 2006, **89**, 172105.
24. N. Park, K. Sun, Z. Sun, Y. Jing and D. Wang, *Journal of Materials Chemistry C*, 2013, **1**, 7333-7338.
25. D. Y. Kim, J. Ryu, J. Manders, J. Lee and F. So, *ACS Applied Materials & Interfaces*, 2014, **6**, 1370-1374.
26. D. Franta, B. Negulescu, L. Thomas, P. R. Dahoo, M. Guyot, I. Ohlídal, J. Mistrík and T. Yamaguchi, *Applied Surface Science*, 2005, **244**, 426-430.

27. J. B. Franklin, B. Zou, P. Petrov, D. W. McComb, M. P. Ryan and M. A. McLachlan, *Journal of Materials Chemistry*, 2011, **21**, 8178-8182.

28. P. F. Carcia, R. S. McLean, M. H. Reilly and G. Nunes, *Applied Physics Letters*, 2003, **82**, 1117-1119.

29. H. Sato, T. Minami, S. Takata and T. Yamada, *Thin Solid Films*, 1993, **236**, 27-31.

30. B. P. Zhang, N. T. Binh, Y. Segawa, K. Wakatsuki and N. Usami, *Applied Physics Letters*, 2003, **83**, 1635-1637.

31. T. Maruyama and S. Arai, *Solar Energy Materials and Solar Cells*, 1993, **30**, 257-262.

32. E. Cicek, R. McClintock, C. Y. Cho, B. Rahnema and M. Razeghi, *Applied Physics Letters*, 2013, **103**, 181113.

33. H. Liu, Z. Zhang, L. Hu, N. Gao, L. Sang, M. Liao, R. Ma, F. Xu and X. Fang, *Advanced Optical Materials*, 2014, **2**, 771-778.

34. A. Knigge, M. Brendel, F. Brunner, S. Einfeldt, A. Knauer, V. Kueller and M. Weyers, *physica status solidi (c)*, 2013, **10**, 294-297.

35. N. V. Nguyen, S. Sayan, I. Levin, J. R. Ehrstein, I. J. R. Baumvol, C. Driemeier, C. Krug, L. Wielunski, P. Y. Hung and A. Diebold, *Journal of Vacuum Science &amp; Technology A*, 2005, **23**, 1706-1713.

36. R. E. Dietz, G. I. Parisot and A. E. Meixner, *Physical Review B*, 1971, **4**, 2302-2310.

37. B. Varghese, M. V. Reddy, Z. Yanwu, C. S. Lit, T. C. Hoong, G. V. Subba Rao, B. V. R. Chowdari, A. T. S. Wee, C. T. Lim and C.-H. Sow, *Chemistry of Materials*, 2008, **20**, 3360-3367.

38. R. Cuscó, E. Alarcón-Lladó, J. Ibáñez, L. Artús, J. Jiménez, B. Wang and M. J. Callahan, *Physical Review B*, 2007, **75**, 165202.

39. M. Burgelman, P. Nollet and S. Degrave, *Thin Solid Films*, 2000, **361–362**, 527-532.

40. H.-M. Chiu and J.-M. Wu, *Journal of Materials Chemistry A*, 2013, **1**, 5524-5534.

41. T. Ghosh and D. Basak, *Journal of Physics D: Applied Physics*, 2009, **42**, 145304.

42. J. P. Kar, S. N. Das, J. H. Choi, Y. A. Lee, T. Y. Lee and J. M. Myoung, *Journal of Crystal Growth*, 2009, **311**, 3305-3309.

43. J.-K. Ho, C.-S. Jong, C. C. Chiu, C.-N. Huang, C.-Y. Chen and K.-K. Shih, *Applied Physics Letters*, 1999, **74**, 1275-1277.

44. C. Soci, A. Zhang, B. Xiang, S. A. Dayeh, D. P. R. Aplin, J. Park, X. Y. Bao, Y. H. Lo and D. Wang, *Nano Letters*, 2007, **7**, 1003-1009.

45. H. Kind, H. Yan, B. Messer, M. Law and P. Yang, *Advanced Materials*, 2002, **14**, 158-160.

46. Z. Zhai, X. Huang, M. Xu, J. Yuan, J. Peng and W. Ma, *Advanced Energy Materials*, 2013, **3**, 1614-1622.

47. P.-N. Ni, C.-X. Shan, S.-P. Wang, X.-Y. Liu and D.-Z. Shen, *Journal of Materials Chemistry C*, 2013, **1**, 4445-4449.

48. M. A. Abbasi, Z. H. Ibupoto, A. Khan, O. Nur and M. Willander, *Materials Letters*, 2013, **108**, 149-152.

**Figure Captions**

**Fig. 1** (a) Cross-section SEM images of the actual device showing various components in the device. AFM images of (b) NiO and (c) ZnO showing the surface morphology. The substrates were annealed at 300 °C and the nanograins are evident from their images.

**Fig. 2** (a) Estimation of the direct energy band gap from ellipsometry measurements (Tauc plot). Both materials have direct band gap. (b) Raman spectroscopy data show various peaks associated with different modes of NiO and ZnO. (c) XRD scans showing diffraction peaks coming from cubic and hexagonal structures of NiO and ZnO, respectively. Both Raman and XRD measurements confirm the formation of metal oxides.

**Fig. 3** (a) Band diagram of p-NiO/n-ZnO at equilibrium and under 1 V reverse bias along with the approximate conduction band edge ($E_c$), valence bad edge ($E_v$) and the Fermi levels for holes ($E_{F,p}$) and electrons ($E_{F,n}$). Under UV illumination, the photogenerated electrons move to ZnO side and holes move to NiO side influenced by the large depletion width due to reverse bias. (b) Diode characteristic of the device: both in dark and UV illumination at 325 nm with 6.5 µW power. The rectifying nature of the diode as well as the photoresponse is evident from the I-V data. The inset illustrates the schematic of the PD showing NiO/ZnO heterojunction along with FTO and Ti/Au metal contacts.

**Fig. 4** Device performance: (a) measured EQE of the PD as a function of applied reverse bias with light illumination through the glass/FTO side. The maximum EQE reaches to 93% at 365 nm with a reverse bias of 1 V. (b) Calculated responsivity (left-axis) and detectivity (right-axis) of the device at 1 V. The actual device is shown as an inset along with the circular arrays Ti/Au contacts. NIST logo can be seen through the transparent oxide films and the metal contacts.

**Fig. 5** (a) Measured EQE of the same device shown in Fig. 4a as a function of applied reverse bias. Here, light is illuminated through Ti/Au contact. The EQE reaches to a maximum value of 55% at 355 nm under 0.8 V. (b) Large area (400 μm × 400 μm) EQE map of the device at zero bias. The photoresponse from the device can be seen with some variation across the measured area of the specimen. (c) Time-resolved photocurrent response to a 20 s light pulse from 325 nm He-Cd laser demonstrating the characteristics transient response of the semiconductors. Dark currents have been subtracted.
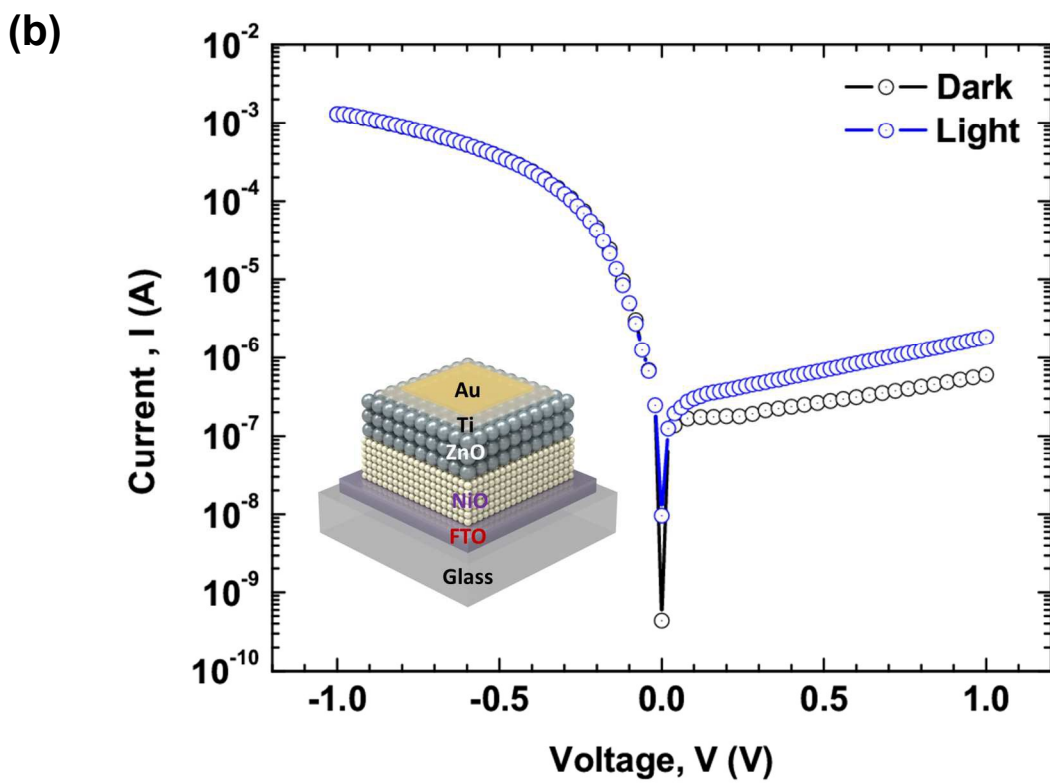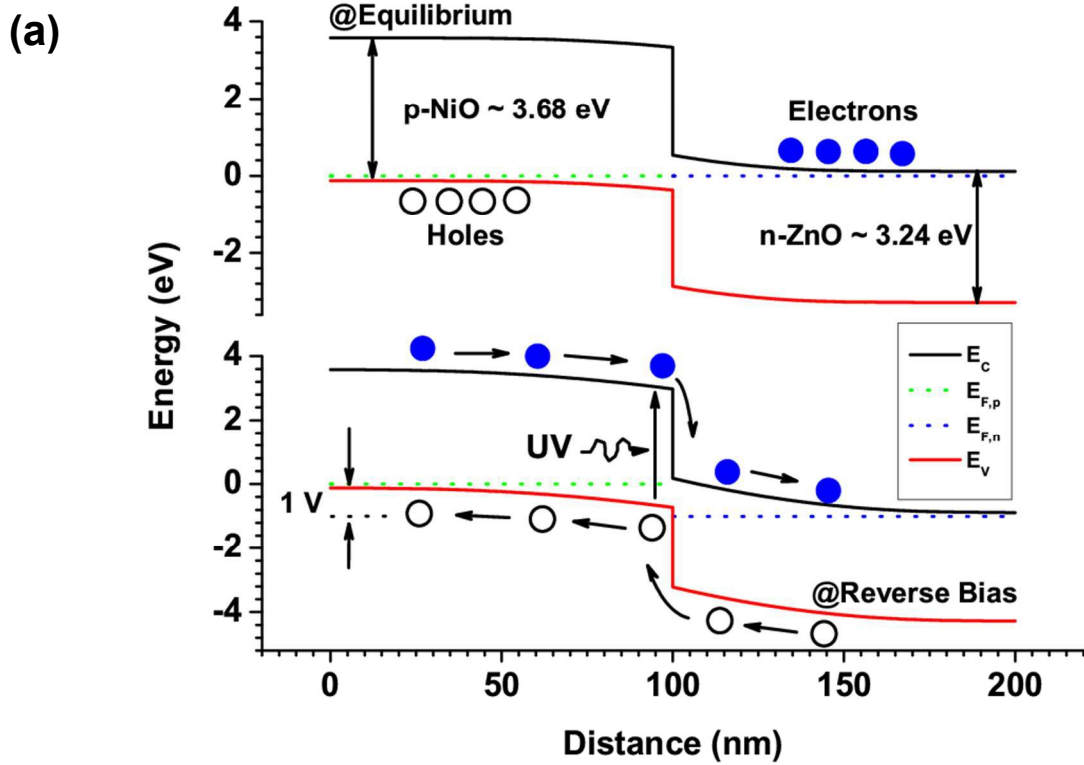
**Figure 1**

**Figure 2**

16

**(a)**



**(b)**



**Figure 3**

17
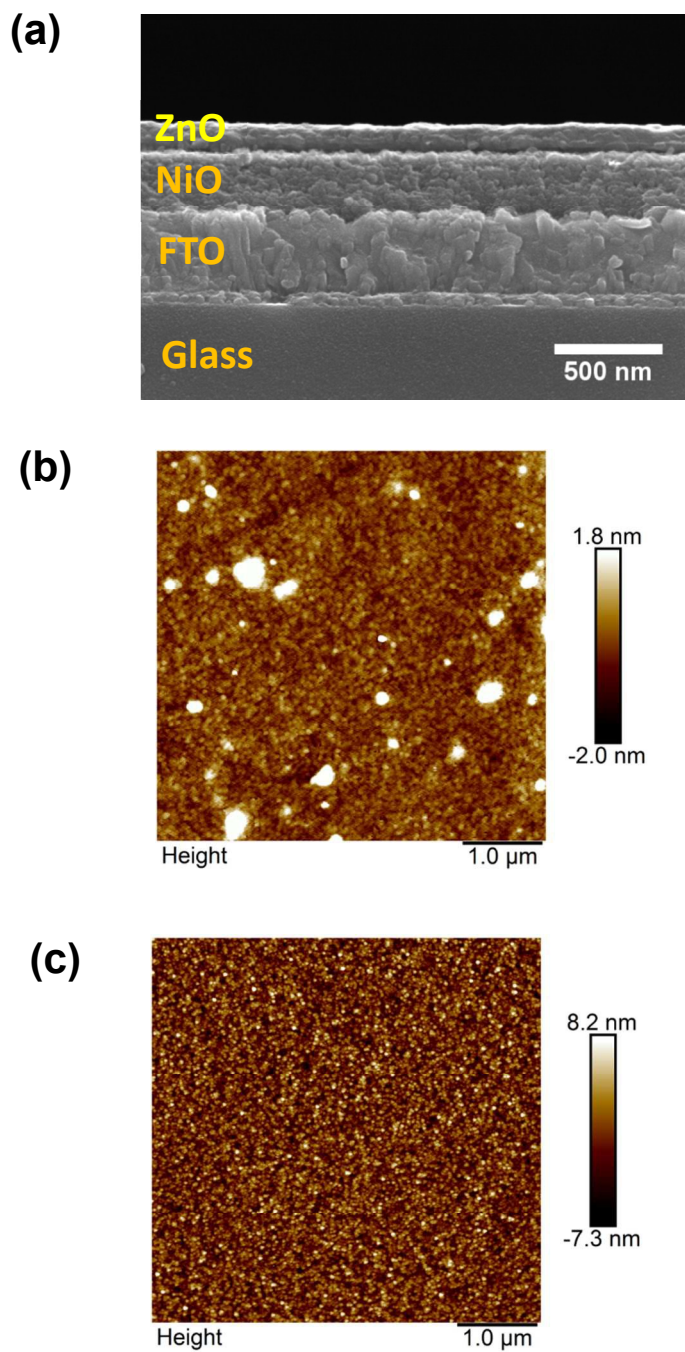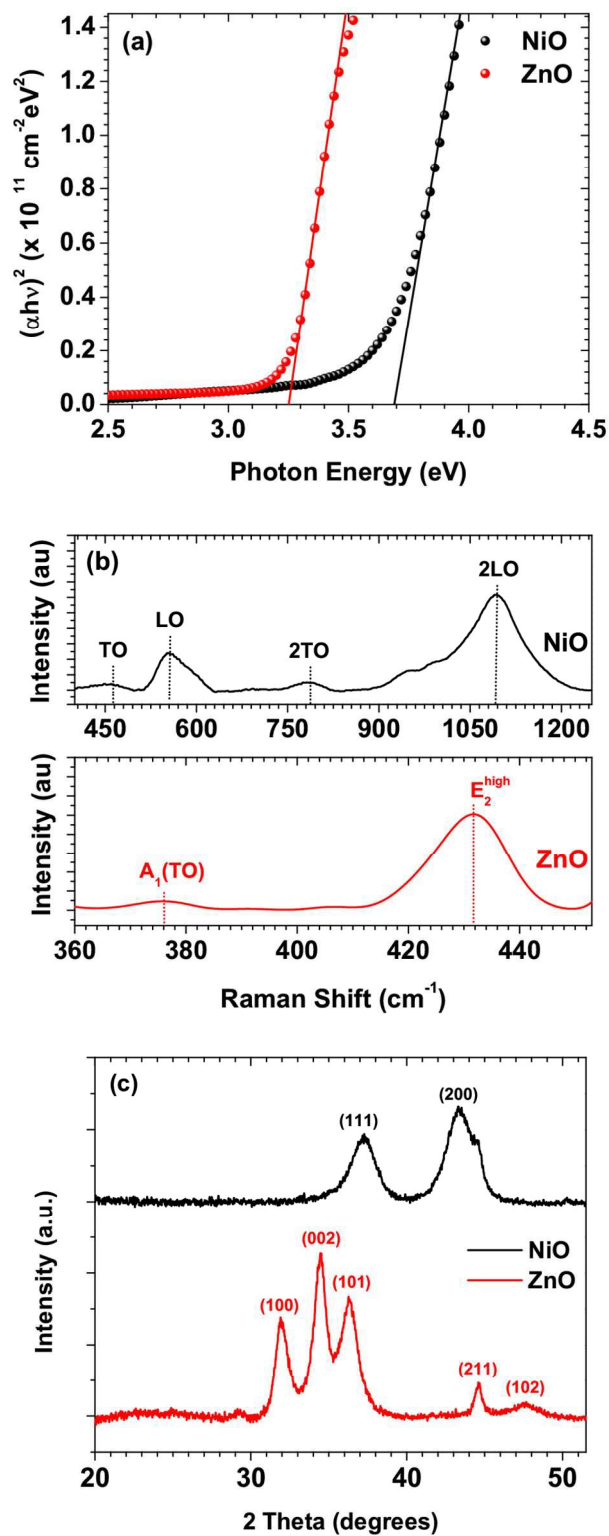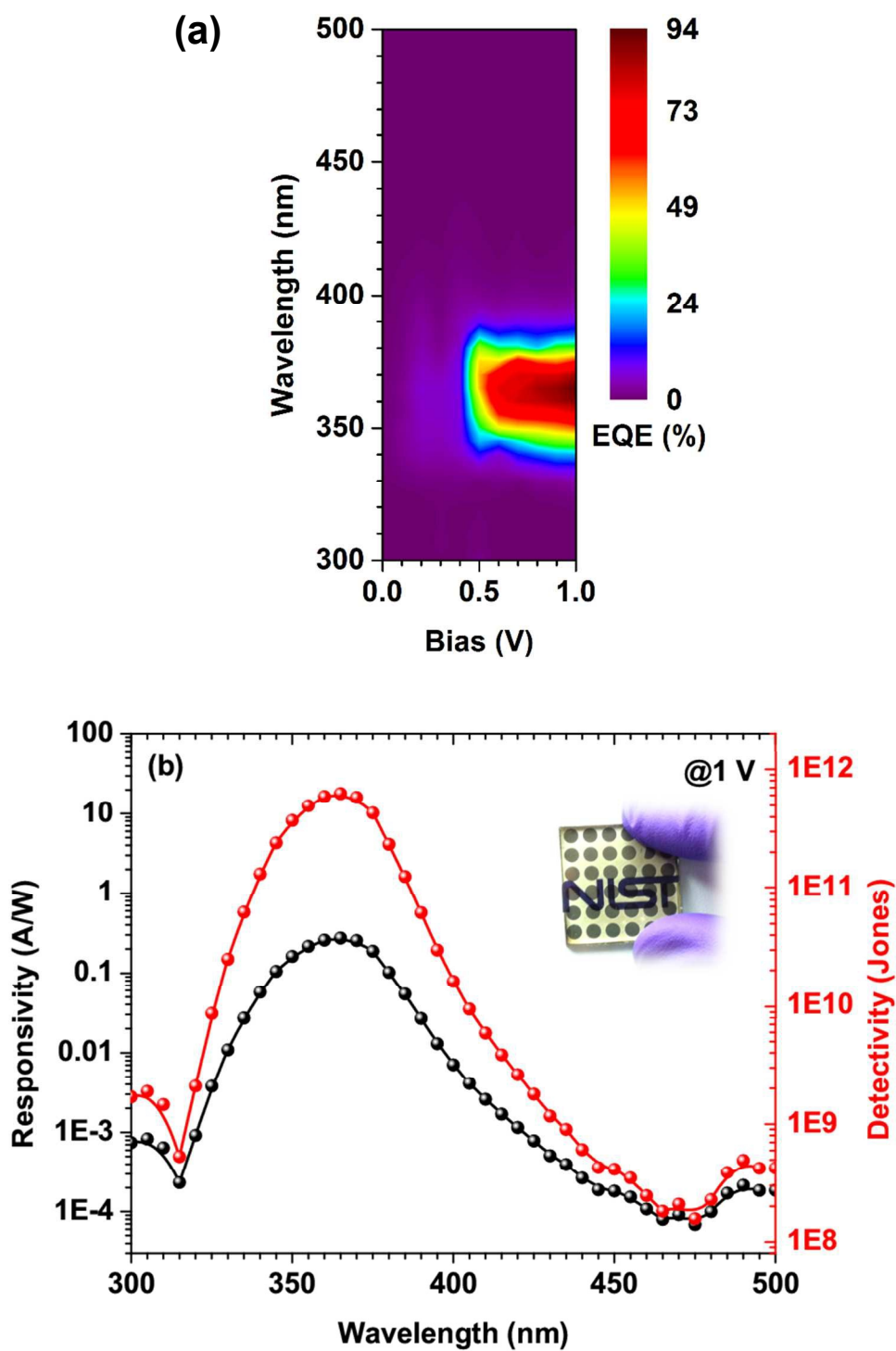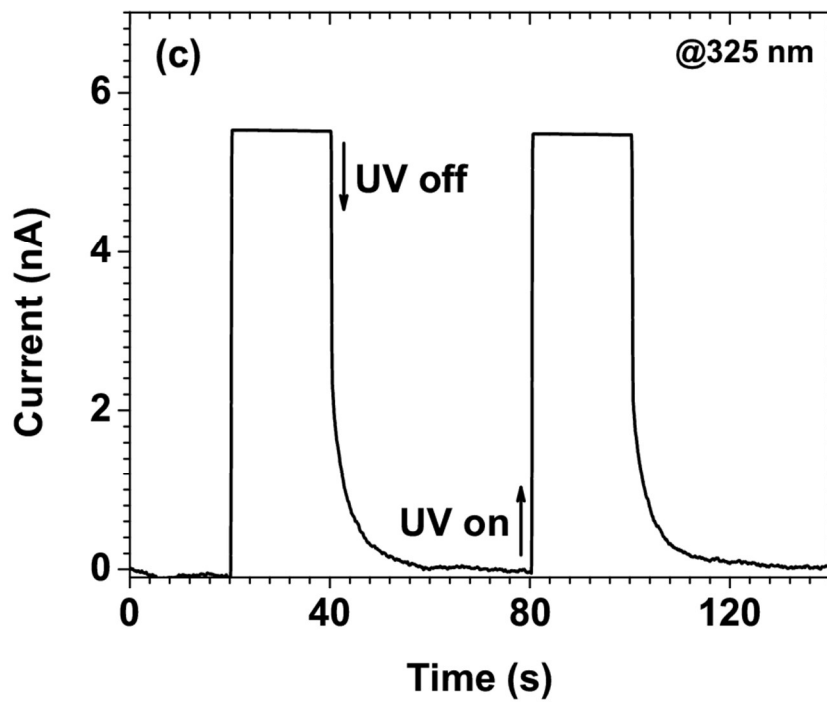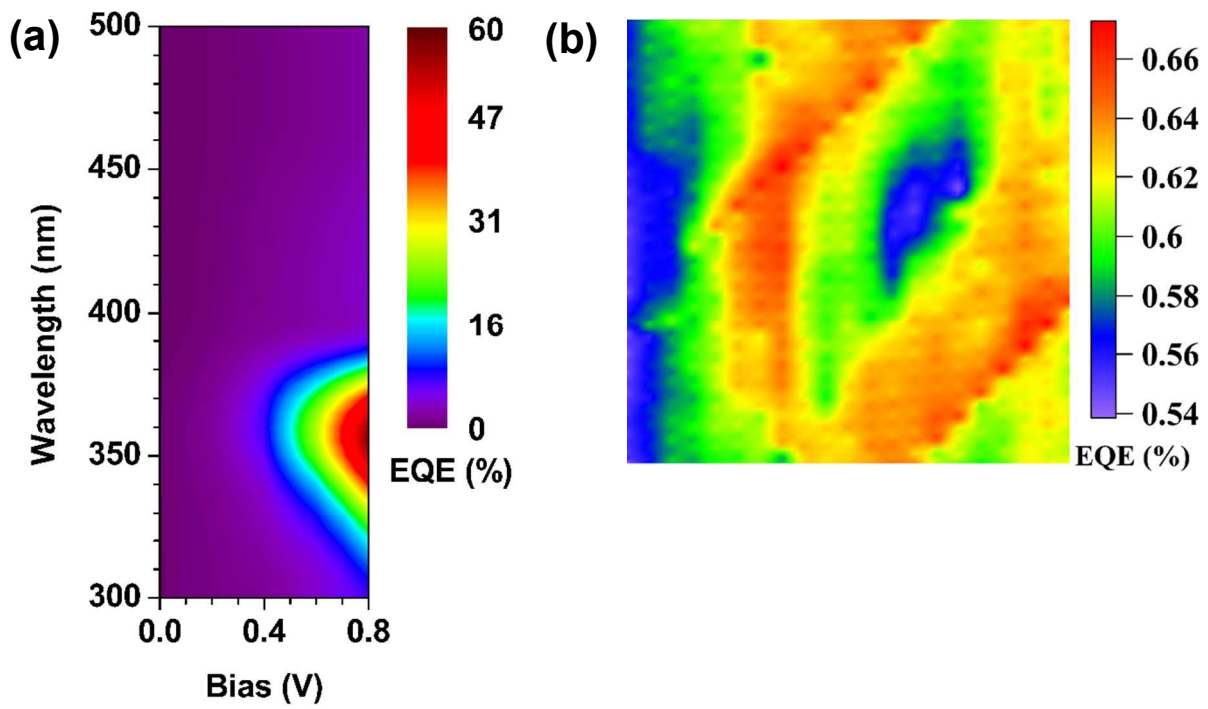
**Figure 4**

**Figure 5**

**Table 1:** Performance matrix of NiO-ZnO based PDs.

| PD Architecture | Bias (V) | EQE (%) | $R_\lambda$ (A/W) | $D^*$ (Jones) | $t_r$ (s) | $t_d$ (s) | Ref. |
|---|---|---|---|---|---|---|---|
| Ni-NiO-ZnO-ITO | 5 | 18 | – | – | – | 37 | [23] |
| In-ZnO-NiO-Au | 0 | – | $0.493m$ | – | 10μ | 30.3μ | [47] |
| FTO-ZnO-NiO-Ag | 3 | – | 3.2 | – | – | 30 | [48] |
| ITO-NiO-ZnO-Al | 1 | 189 | 10.2 | $1 \times 10^{12}$ | 0.2 | 0.18 | [25] |
| ITO-NiO-ZnO-Al | 5 | 88 | 21.8 | $1.6 \times 10^{12}$ | – | – | [24] |
| **FTO-NiO-ZnO-Ti-Au** | **1** | **94** | **0.28** | $\mathbf{6.3 \times 10^{11}}$ | **0.28** | **5.4** | **This work** |